Impedance-matching acoustic bend composed of perforated plates and side pipes

Yuzhen Yang, Han Jia, Wenjia Lu, Zhaoyong Sun, and Jun Yang

Impedance-matching acoustic bend composed of perforated plates and side pipes

Yuzhen Yang,[1,2] Han Jia,[1,2,3] Wenjia Lu,[1,2] Zhaoyong Sun,[1,2] and Jun Yang[1,2,3,a]

[1]*Key Laboratory of Noise and Vibration Research, Institute of Acoustics, Chinese Academy of Sciences, Beijing 100190, People's Republic of China*
[2]*University of Chinese Academy of Sciences, Beijing 100049, People's Republic of China*
[3]*State Key Laboratory of Acoustics, Institute of Acoustics, Chinese Academy of Sciences, Beijing 100190, People's Republic of China*

In this article, we propose a design for an impedance-matching acoustic bend. The bending structure is composed of sub-wavelength unit cells containing perforated plates and side pipes that allow the mass density and the bulk modulus of each unit cell to be tuned simultaneously. The refractive index and the impedance of the acoustic bend can therefore be modulated simultaneously to guarantee both the bending effect and high acoustic transmission. The results of simulation of the sound pressure field distribution show that the bending effect of the proposed impedance-matching acoustic bend is very good. Transmission spectra are calculated for both the impedance-matching acoustic bend and an acoustic bend composed of the perforated plates alone for comparison. The results indicate that the impedance-matching acoustic bend successfully improves the impedance ratio while also obviously increasing the transmission. *Published by AIP Publishing.*
[http://dx.doi.org/10.1063/1.4996848]

INTRODUCTION

Acoustic metamaterials basically cover all artificial materials with periodic or pseudo-periodic sub-wavelength unit cells that mainly derive their responses from their geometrical structures rather than their chemical components. By adjusting the structural parameters of acoustic metamaterials, it is possible to obtain some extraordinary acoustic parameters that cannot be realized easily using natural materials; these parameters include negative mass density and negative bulk modulus values,[1–5] anisotropic mass density tensors,[6,7] and anisotropic elasticity tensors.[8] In previous studies of acoustic metamaterials, a variety of amazing phenomena have been discovered,[9–19] including negative refraction,[9–11] rainbow trapping,[12–14] and acoustic cloaking.[15–19] The acoustic bending effect is one of these interesting phenomena.

In a conventional waveguide containing a bend, reflections from the side walls will distort the wavefront and the wave modes in the waveguide will then become chaotic. A great deal of research work has been conducted on optical bends[20–25] to solve this problem. Research on acoustic bends is also important for a variety of fields, including sound absorption and detection in pipelines in industrial applications. Wu and Chen used a two-dimensional graded sonic crystal to realize an acoustic bending waveguide with a wide operating frequency range.[26] Wang *et al.* designed an acoustic bending waveguide that used an anisotropic density-near-zero metamaterial.[27] The surface waves on the input and output interfaces of the anisotropic density-near-zero metamaterial cause the sound energy flow to be redistributed and perfectly matched with the modes that are propagating inside the waveguide.

Baboly *et al.* introduced an isolated single-mode 90°-bend phononic crystal waveguide.[28] A phononic crystal that consisted of an array of circular air holes in an aluminum substrate was used, and waveguides were created by introducing line defects into the lattice.

In our previous research, an acoustic bend that was composed of perforated plates (ABPP) was proposed to manipulate sound waves inside a two-dimensional waveguide.[29] However, impedance mismatching caused reflections from the incident surface and the exit surface of the ABPP. In this article, an impedance-matching acoustic bend (IMAB) design that avoids these reflections from the side walls and enhances acoustic energy transmission is proposed. We introduce new complex unit cells containing perforated plates and side pipes in which the mass density and the bulk modulus can be tuned simultaneously. The proposed structure successfully meets both the refractive index distribution and acoustic impedance requirements for the acoustic bend. As a result, the IMAB can manipulate the sound propagation inside the waveguide effectively while maintaining high transmission over both a wide angular range and a relatively wide frequency range.

THEORY AND DESIGN

The proposed IMAB is an arc-shaped waveguide with inner radius r_1, outer radius r_2, and a bending angle of 0.5π, as shown in Fig. 1(a). The sound waves are intended to travel in the circumferential direction (indicated by the bold solid curve with the arrow). It is known that acoustic wave propagation can be manipulated by appropriate design of the refractive index distribution of the medium. In an acoustic bending structure, the phase variation remains the same at different radial positions, and the refractive index distribution is given by $n = A/r$.[21] In addition to the refractive

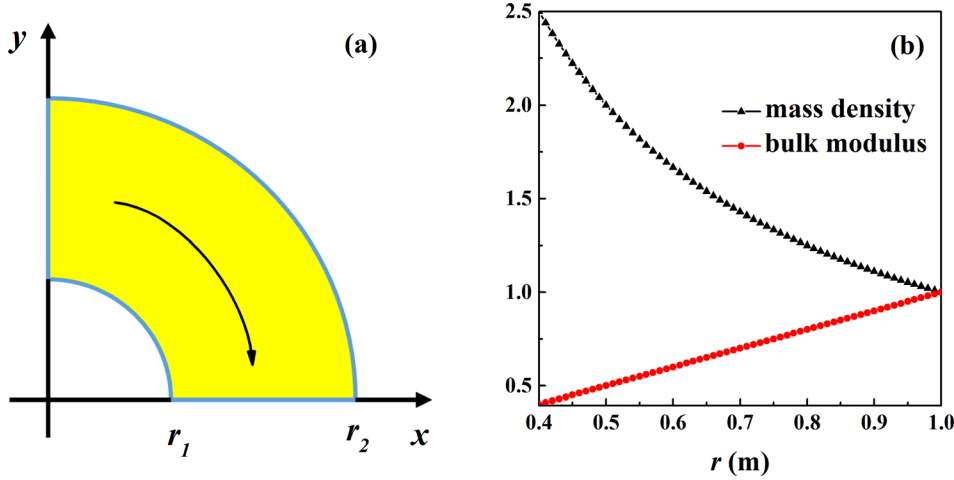a)Author to whom correspondence should be addressed: jyang@mail.ioa.ac.cn

FIG. 1. (a) Schematic of the acoustic bend structure. The bold solid curve with the arrow denotes the wave propagation direction. (b) Relationship curves for the mass density and the bulk modulus with respect to the radial position r.

index, the acoustic impedance also affects the sound propagation characteristics. When both the refractive index and impedance matching are taken into consideration, they should be expressed as follows:

$$\begin{cases} n = \dfrac{A}{r} \\ Z = Z_0, \end{cases} \quad (1)$$

where A is a constant, r is the radial position of the acoustic bend, and Z_0 is the acoustic impedance of air. Equation (1) indicates that the refractive index varies along the radial direction while the impedance remains constant. The bending effect of the acoustic bend is thus derived from this continuous variation of the refractive index, which is inversely proportional to the radial position in the structure. The refractive index n and the acoustic impedance Z are both functions of the relative mass density ρ and the relative bulk modulus B as shown in Eq. (2)

$$\begin{cases} n = \sqrt{\dfrac{\rho}{B}} \\ Z = \sqrt{\rho B} * Z_0 \end{cases} \quad (\rho = \rho_{eff}/\rho_0 \ B = B_{eff}/B_0), \quad (2)$$

where ρ_0 and B_0 are the mass density and the bulk modulus of air, respectively, and ρ_{eff} and B_{eff} are the effective mass density and the effective bulk modulus of the IMAB, respectively. By combining Eqs. (1) and (2), the spatial distributions of the relative mass density and the relative bulk modulus can then be expressed as follows:

$$\begin{cases} \rho = \dfrac{1}{r} \\ B = r, \end{cases} \quad (3)$$

where we use $A = 1$ for simplicity. Equation (3) shows that the distributions of the mass density and the bulk modulus are both functions of the radial position. The mass density is inversely proportional to the radial position, while the bulk modulus is directly proportional to the radial position. Figure 1(b) shows the curves for the relationships of the mass density and the bulk modulus with the radial position r. The line of filled triangles shows the variation of the mass density,

while the line of solid circles shows the variation of the bulk modulus.

In our design, the inner and outer radii of the bending structure are $r_1 = 0.4$ m and $r_2 = 0.99$ m, respectively, with a bending angle of 0.5π. To realize the prototype structure using acoustic metamaterials, the bending structure is divided into 59 arc-shaped layers with identical 10 mm widths along the radial direction because the mass density and the bulk modulus vary with the changes of the radial position. Each layer is considered to be composed of a homogeneous material with physical parameters that are equal to their values at the center line of the layer. Based on the radial position of the layer's center line, the mass density and the bulk modulus can then be calculated using Eq. (3). Each layer is then divided into 30 periodic units along its circumferential direction. As a result, the entire structure is divided into 59×30 arc-shaped unit cells. The angle and the width of each unit cell are 3° and 10 mm, respectively. The length d of the unit cell is the average arc length, which is a function of the radial position r. In fact, the practical acoustic bend structure is a quasi-two-dimensional structure with a height h' of 10 mm, because the component unit cells have a specific height of 10 mm. The arc-shaped unit cell could be considered to be a cuboid during calculation of the acoustic parameters of the cell in the following because of its small angle, width, and length.

In our previous research, a unit cell with a perforated plate [inset of Fig. 2(a)] was used to modulate the mass density of the medium by varying the radius of the hole.[29] This perforated plate can be regarded as a tiny pipe with an impedance of $Z' = \rho_0 c_0 / S$. In this work, the variation of the sectional area of the hole is equivalent to the variation of the effective mass density, where a larger radius leads to a smaller effective mass density. From the work of Lee and Wright, it is known that a unit cell with a side pipe [inset of Fig. 2(c)] could be used to modulate the bulk modulus of the medium by varying the side pipe's height.[5] The change in pressure in the main pipe is $p = -B_0(\Delta V - \Delta V_h)/V$, and the change in pressure in the side pipe is $p_h = -B_0 \Delta V_h / V_h$. Here, V and V_h represent the volumes of the main pipe and the side pipe, respectively, while ΔV and ΔV_h are the small changes in the main pipe and side pipe volumes, respectively. The effective bulk modulus is only dependent on the observable volume
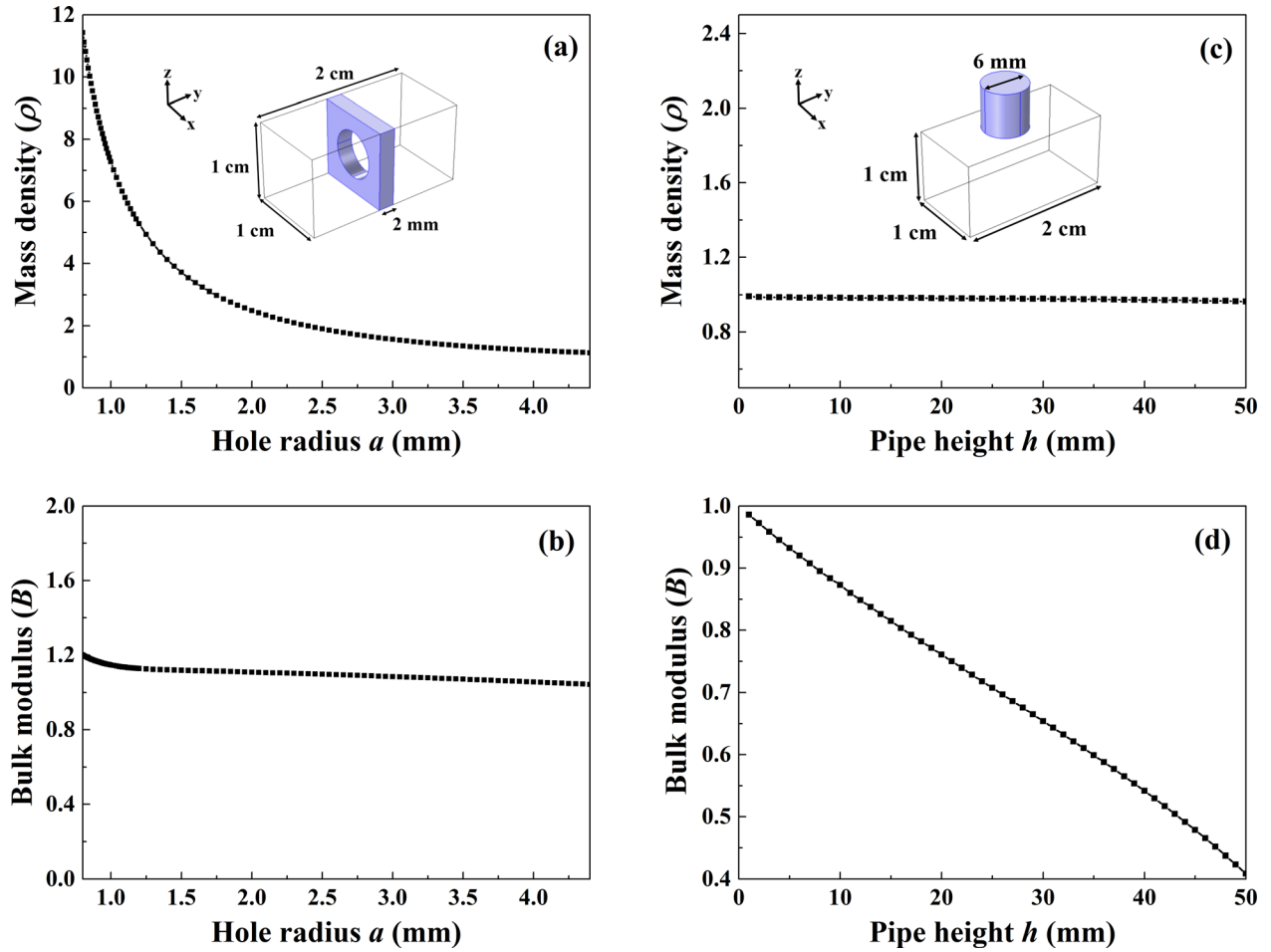
FIG. 2. Relationship curves for (a) and (c) the mass density and (b) and (d) the bulk modulus with respect to the geometrical parameters of the two different unit cells; the left panel is for the unit cell with the perforated plate [inset in (a)] and the right panel is for the unit cell with the side pipe [inset in (c)].

change ΔV, and thus, the formula becomes $p = -B_{eff}\Delta V/V$. Because $p = p_h$, the effective bulk modulus is given by $B_{eff} = B_0/(1 + V_h/V)$, which means that as the height of the side pipe increases, the effective bulk modulus decreases.

The effective parameters of the two unit cells are calculated using the well-developed retrieval method.[30] In this retrieval method, the effective refractive index n and impedance Z are obtained from the reflection and transmission coefficients of a plane wave that is normally incident on the metamaterial. The effective mass density ρ_{eff} and bulk modulus B_{eff} are then calculated based on n and Z. This means that the metamaterial is effectively replaced by a homogeneous fluid material that presents the same amplitude and phase of the reflection and transmission coefficients. In the calculations, the incident plane wave is at a frequency of 1200 Hz, which is the central working frequency of the designed prototype. Each unit cell has a cuboid geometry with a length of 20 mm and the width and height of 10 mm. In the unit cell with the perforated plate, the thickness of the perforated plate is 2 mm and the hole radius is represented by a. In the unit cell with the side pipe structure, the radius of the side pipe is 3 mm and the pipe height is h. The sound waves are intended to travel in the y direction, i.e., in the circumferential direction of the acoustic bending structure. Therefore, the variations in the refractive index and the impedance of the unit cell in the

orthogonal x direction have no effect on the acoustic propagation, and only the acoustic parameters in the y direction have to be modulated. We first study the acoustic parameters of the unit cell with the perforated plate. The relationship between the mass density and the hole radius is shown in Fig. 2(a), while the relationship between the bulk modulus and the hole radius is shown in Fig. 2(b). The mass density clearly decreases from 11.4 to 1.1 when the hole radius changes from 0.8 mm to 4.4 mm. In contrast, the bulk modulus remains almost constant at approximately 1. We then study the acoustic parameters of the unit cell with the side pipe. The relationship between the mass density and the pipe height is shown in Fig. 2(c), while the relationship between the bulk modulus and the pipe height is shown in Fig. 2(d). The figures show that the mass density of the unit cell with the side pipe remains almost identical at approximately 1 when the pipe height varies. However, the bulk modulus decreases from 0.99 to 0.41 when the height increases from 1 mm to 50 mm. These results verify that the unit cell with the perforated plate can modulate the mass density while the unit cell with the side pipe can modulate the bulk modulus separately. We therefore combine these two types of unit cells to obtain the new complex unit cell shown in Fig. 3(c), which can then be used to modify the mass density and the bulk modulus simultaneously.
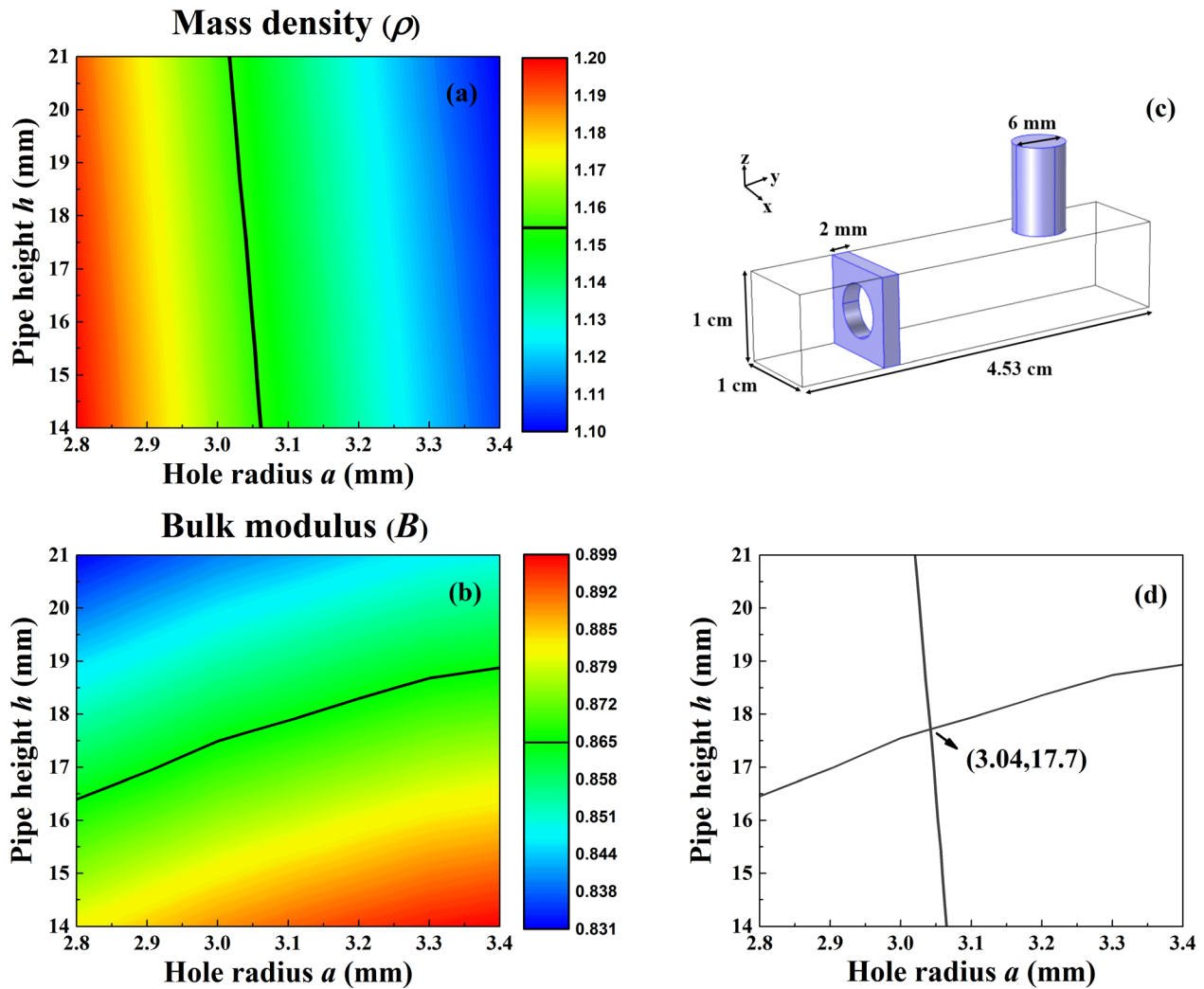
FIG. 3. Distribution maps of (a) mass density and (b) bulk modulus for various hole radii and pipe heights. (c) Schematic of the complex unit cell. (d) Overlapping map of Figs. 3(a) and 3(b).

While the perforated plate and the side pipe affect each other weakly, the mapping method that is used to scan the hole radius and the pipe height at the same time is introduced to obtain the exact geometrical parameters of the complex unit cells. The process of calculation of the geometrical parameters of the unit cells with radial position r of 0.865 m is given as an example. The mass density distribution map at 1200 Hz for different hole radii and different pipe heights is shown in Fig. 3(a). The distribution map for the bulk modulus at 1200 Hz is shown in Fig. 3(b). The x axis represents the variation of the hole radius, while the y axis represents the variation of the pipe height. The black lines shown in the maps indicate the required values of the mass density $\rho = 1.156$ and the bulk modulus $B = 0.865$ that were obtained using Eq. (3). It is then simple to obtain the exact geometrical parameters by overlapping the two maps, as shown in Fig. 3(d). The precise coordinate values at the intersection of the two black lines are the required parameters. The rainbow colors for the other parameter values in Figs. 3(a) and 3(b) are set to be transparent to ensure the clarity of the overlapping map. Figure 3(d) shows that the values at the intersection are $a = 3.04$ mm and $h = 17.7$ mm. The geometrical

parameters of the unit cells where $r = 0.865$ m (i.e., the unit cells of the 47th layer) are therefore $a = 3.04$ mm and $h = 17.7$ mm.

The various unit cells of other 58 layers along the radial direction are retrieved one by one using the method described above. The detailed geometrical parameters of the unit cells in each layer are shown in Fig. 4(a). In this figure, the x axis represents the radial positions, while the left y axis represents the radii of the perforated plates and the right y axis represents the side pipe heights. Over the range from the center to the periphery along the radial direction, the hole radii increase from 1.73 mm to 4.69 mm, as indicated by the black triangular dots, while the heights of the side pipes decrease from 48.7 mm to 2.8 mm, as indicated by the red circular dots. The entire IMAB structure when configured using all the calculated unit cells is as shown in Fig. 4(b), and the inset shows an enlarged part of the structure that is composed of 12 unit cells. The maximum period d of the outermost layer is 52 mm, which makes the unit cell at least five times smaller than the wavelength for frequencies under 1300 Hz. Intuitively, this arrangement allows for a smooth bending effect because the medium can be assumed to be
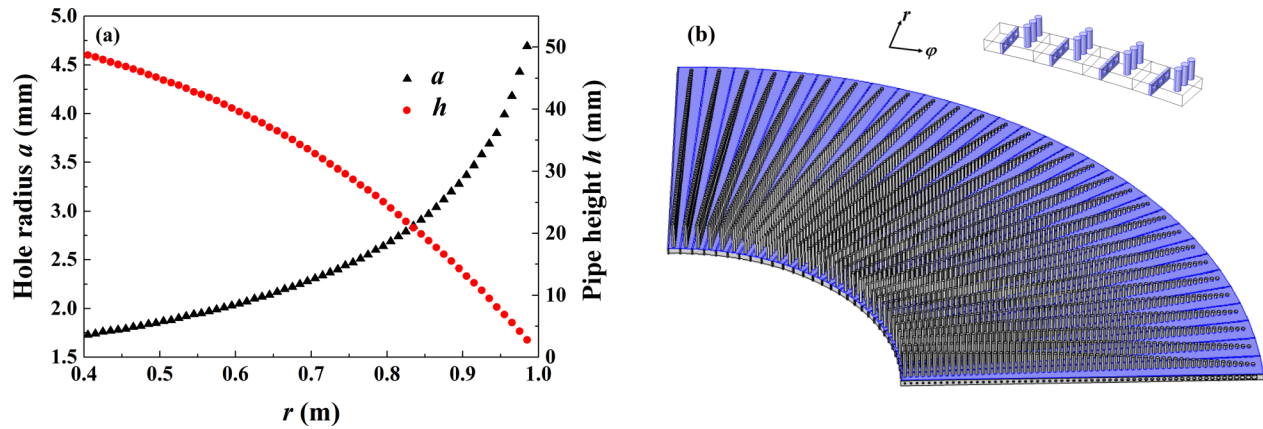
FIG. 4. (a) Distributions of hole radius a and pipe height h with respect to radial position r at 1200 Hz. (b) Schematic of the practical acoustic bend structure.

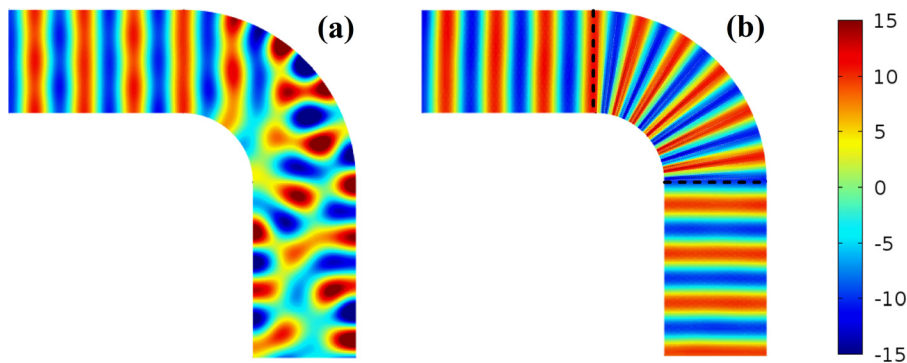
FIG. 5. Sound pressure field distributions at 1200 Hz of (a) empty bending waveguide and (b) bending waveguide with the IMAB with an angle of 90°; black dashed lines indicate the incident surface and the exit surface of the IMAB.

homogeneous with the criterion $d \leq \lambda/5$. The upper frequency limit can easily be extended to a higher frequency by reducing the sizes of the unit cells, i.e., by dividing the structure into more layers with more unit cells in each layer.

DISCUSSION

The performance of the proposed IMAB was simulated using the finite element method. An arc-shaped waveguide without an acoustic bend was first simulated, and the result is shown in Fig. 5(a). The height of this waveguide is 10 mm, and its width is 590 mm. A plane wave at 1200 Hz was emitted from the left boundary and entered normally into the bend area. However, the sound mode was distorted when the wave passed through the bend area. This distortion was derived from undesired reflections from the hard walls. As shown in Fig. 5(b), the IMAB was inserted into the bend area and the geometrical parameters of the IMAB that were configured for the simulation were the same as those given in Fig. 4(a). The incident surface and the exit surface of the IMAB are indicated by the black dashed lines. The sound pressure field distribution shown in Fig. 5(b) demonstrates that the IMAB protects the mode in the waveguide effectively and guarantees that the wavefront shape is maintained when sound propagates through the bend area.

The energy transmission of the IMAB was then calculated and is presented as the line of black squares in Fig. 6. The figure shows that the transmission remains high over a relatively wide frequency range from 1100 Hz to 1300 Hz, which is result of the impedance matching. For comparison,

the transmission curve for the ABPP was also calculated and is presented as the line of red circles in Fig. 6. The transmission of the ABPP decreases because of reflections at both the incident surface and the exit surface caused by impedance mismatching. The figure shows that the transmission of the IMAB structure is remarkably higher than that of the ABPP. The transmission dip of the former structure is 0.93 while the corresponding transmission dip of the latter is 0.72, representing an increase of 29%. The transmission dip values that occur closest to 1200 Hz are used because the center frequency of the prototype is 1200 Hz.

These transmission curves fluctuate because of Fabry-Perot resonance. In the proposed system, the sound waves
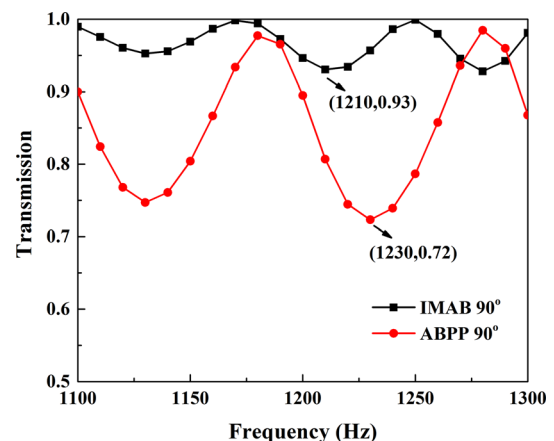

FIG. 6. Transmission curves of the IMAB and the ABPP with angles of 90°.

propagate along the circumferential direction of the acoustic bend and remain perpendicular to the radial direction at all points. Additionally, the phase variation remains unchanged throughout the different layers, although both the length of the route and the refractive index vary with the radial position. In a manner similar to sound waves propagating through a planar interlayer, the energy transmission can be expressed as follows:

$$t_I = \frac{4}{4\cos^2(k_2 D) + (R_{12} + R_{21})^2 \sin^2(k_2 D)}$$
$$R_{12} = \frac{R_2}{R_1} \quad R_{21} = \frac{R_1}{R_2}, \tag{4}$$

where R_1 and R_2 are the impedances of the background medium and the interlayer medium, respectively, and D is the interlayer length. In this work, R_1 and R_2 are the impedances of the air and the acoustic bend, respectively, while D is the effective length of the acoustic bend in view of the arc shape of the bend structure. The transmission dip appears when the interlayer length is equal to an odd multiple of 1/4 of the acoustic wavelength (i.e., where $k_2 D = (2n - 1) \times (\pi/2)$) and the transmission can then be simplified as follows:

$$t_I = \frac{4}{(R_{12} + R_{21})^2}. \tag{5}$$

The impedance ratio R_{12} can be calculated easily by substituting the transmission dip values into Eq. (5). The calculated impedance ratio for the ABPP is 1.80, while the calculated impedance ratio for the IMAB is 1.31. The impedance ratio thus improves by 27% when using the IMAB.

The IMABs with angles of 45° and 120° were also simulated in this work. The bending effect in these IMABs is good as that in the IMAB with the angle of 90°, as indicated

by the sound pressure field distributions shown in Figs. 7(a) and 7(b). The modes of the plane waves are maintained perfectly after the sound waves pass through the bend areas with the different angles. The energy transmission curves for the acoustic bends with angles of 45° and 120° are shown in Figs. 7(c) and 7(d). The transmission of the IMAB is still much higher than the transmission of the ABPP in both cases. For single frequency signals, such as signals at 1210 Hz for the IMAB and 1230 Hz for the ABPP, the transmission values of the IMABs with the different angles vary little and are all higher than 0.9, while the transmission values for the ABPPs with their different angles vary widely because of severe impedance mismatching. These results indicate that the IMAB works effectively over a wide angular range.

CONCLUSION

In conclusion, a metamaterial-based IMAB is designed and simulated. A complex unit cell structure with a perforated plate and a side pipe is used in the design to manipulate the mass density and the bulk modulus of the medium simultaneously. The well-developed retrieval method is used to obtain the effective mass density and the effective bulk modulus for each of the unit cells, and a mapping method is introduced to obtain the exact geometrical parameters of the complex unit cells. Simulation results for the proposed acoustic bends show that the IMAB protects the wave mode during transmission in the waveguide and effectively guarantees the wavefront shape. Additionally, the great improvement in the impedance ratio of the IMAB maintains high energy transmission spectra over a wide angular range and a relatively wide operating frequency range from approximately 1100 Hz to 1300 Hz. As above advantages, the proposed design for the IMAB may have great potential applications in sound absorption and detection in pipelines.
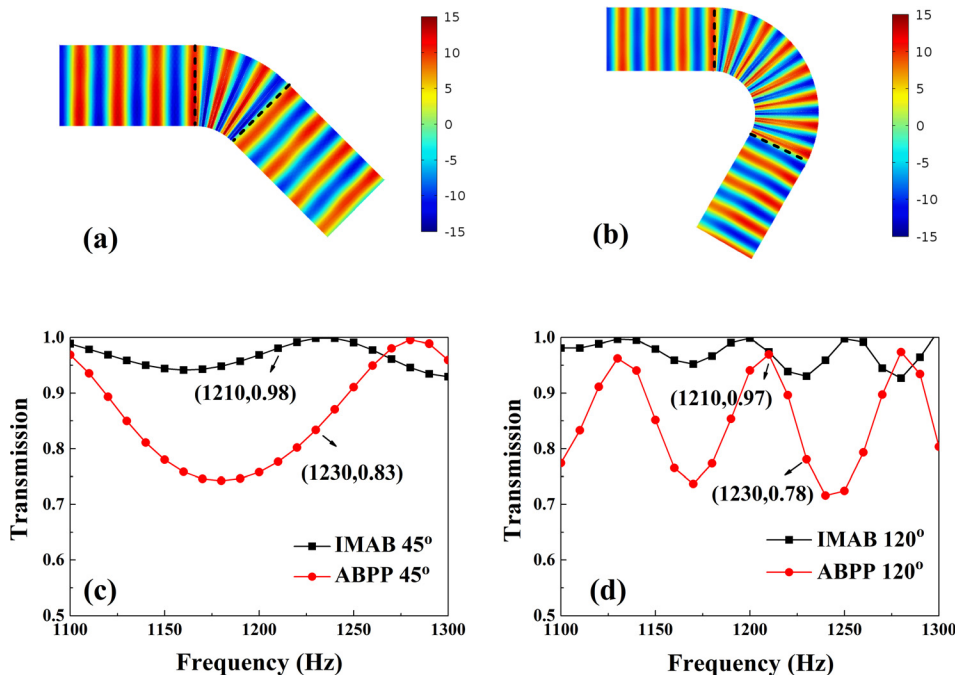

FIG. 7. Sound pressure field distributions at 1200 Hz of IMABs with angles of (a) 45° and (b) 120°. Transmission curves for acoustic bends with angles of (c) 45° and (d) 120°.

ACKNOWLEDGMENTS

[1]J. Li and C. T. Chan, Phys. Rev. E **70**, 055602 (2004).
[2]Y. Ding, Z. Liu, C. Qiu, and J. Shi, Phys. Rev. Lett. **99**, 093904 (2007).
[3]S. H. Lee, C. M. Park, M. S. Yong, G. W. Zhi, and C. K. Kim, Phys. Lett. A **373**, 4464 (2009).
[4]S. H. Lee, C. M. Park, Y. M. Seo, Z. G. Wang, and C. K. Kim, Phys. Rev. Lett. **104**, 054301 (2010).
[5]S. H. Lee and O. B. Wright, Phys. Rev. B **93**, 024302 (2016).
[6]W. Akl and A. Baz, J. Appl. Phys. **111**, 024907 (2012).
[7]C. Liu, X. Xu, and X. Liu, Appl. Phys. Lett. **106**, 081912 (2015).
[8]Y. Chen, X. N. Liu, and G. K. Hu, Sci. Rep. **5**, 15745 (2015).
[9]L. Feng, X. P. Liu, M. H. Lu, Y. B. Chen, Y. W. Mao, J. Zi, Y. Y. Zhu, S. N. Zhu, and N. B. Ming, Phys. Rev. Lett. **96**, 014301 (2006).
[10]S. Peng, X. Mei, P. Pang, M. Ke, and Z. Liu, Solid State Commun. **149**, 667 (2009).
[11]S. Zhang, L. Yin, and N. Fang, Phys. Rev. Lett. **102**, 194301 (2009).
[12]J. Zhu, Y. Chen, X. Zhu, F. J. Garcia-Vidal, X. Yin, W. Zhang, and X. Zhang, Sci. Rep. **3**, 1728 (2013).
[13]X. Ni, Y. Wu, Z. G. Chen, L. Y. Zheng, Y. L. Xu, P. Nayar, X. Liu, M. H. Lu, and Y. F. Chen, Sci. Rep. **4**, 7038 (2014).
[14]H. Jia, M. Lu, X. Ni, M. Bao, and X. Li, J. Appl. Phys. **116**, 124504 (2014).
[15]B. I. Popa and S. A. Cummer, Phys. Rev. B **83**, 224304 (2011).
[16]X. L. Zhang, X. Ni, M. H. Lu, and Y. F. Chen, Phys. Lett. A **376**, 493 (2012).
[17]W. Hu, Y. Fan, P. Ji, and J. Yang, J. Appl. Phys. **113**, 024911 (2013).
[18]J. Zhu, T. Chen, Q. Liang, and X. Wang, J. Appl. Phys. **116**, 164906 (2014).
[19]L. Zigoneanu, B. I. Popa, and S. A. Cummer, Nat. Mater. **13**, 352 (2014).
[20]W. X. Jiang, T. J. Cui, X. Y. Zhou, X. M. Yang, and Q. Cheng, Phys. Rev. E **78**, 066607 (2008).
[21]Z. L. Mei and T. J. Cui, J. Appl. Phys. **105**, 104913 (2009).
[22]Z. L. Mei and T. J. Cui, Opt. Express **17**, 18354 (2009).
[23]Z. L. Mei, J. Bai, and T. J. Cui, J. Phys. D: Appl. Phys. **43**, 55404 (2010).
[24]W. Ding, D. Tang, Y. Liu, and L. Chen, Appl. Phys. Lett. **96**, 041102 (2010).
[25]B. B. Oner, M. Turduev, and H. Kurt, Opt. Lett. **38**, 1688 (2013).
[26]L. Y. Wu and L. W. Chen, J. Appl. Phys. **110**, 114507 (2011).
[27]Y. Y. Wang, E. L. Ding, X. Z. Liu, and X. F. Gong, Chin. Phys. B **25**, 124305 (2016).
[28]M. G. Baboly, A. Raza, J. Brady, C. M. Reinke, Z. C. Leseman, and I. El-Kady, Appl. Phys. Lett. **109**, 183504 (2016).
[29]W. Lu, H. Jia, Y. Bi, Y. Yang, and J. Yang, J. Acoust. Soc. Am. **142**, 84 (2017).
[30]V. Fokin, M. Ambati, C. Sun, and X. Zhang, Phys. Rev. B: Condens. Matter **76**, 144302 (2007).